Wind-Tunnel Investigation of the ILCA 7 MKII Sail in Downwind Conditions

Journal of Sailing Technology 2023, volume 8, issue 1, pp. 118-142.
The Society of Naval Architects and Marine Engineers.

Wind-Tunnel Investigation of the ILCA 7 MKII Sail in Downwind Conditions

Gustaf Magnander
RISE Research Institutes of Sweden, SSPA Maritime Center, Chalmers University of Technology, Sweden, gustaf.magnander@ri.se

Lars Larsson
Chalmers University of Technology, Sweden.

Manuscript received July 20, 2023; revision received October 4, 2023; accepted October 7, 2023.

Abstract. Aerodynamic coefficients from wind-tunnel tests are presented for the ILCA 7 in all six degrees of freedom. Two apparent wind speeds are considered: a light wind case corresponding to 4 m s^{-1} at full scale and a strong wind case corresponding to 7 m s^{-1}. The light wind tests comprise five apparent wind angles, seven sheet angles, three kicker trims and three heel angles. For the strong wind case the dinghy is assumed sailing upright and only dead downwind, but with four sheet angles and three kicker trims. The scale is $1/7$, which gives a reasonable blockage in the wind-tunnel. Blockage corrections are obtained using CFD. Correct scaling of the sail stretch, and mast bend is achieved with the full-scale sail cloth and a solid stainless-steel mast exposed to a wind speed $\sqrt{7}$ times larger than at full-scale. However, the Reynolds number is $\sqrt{7}$ times smaller. The main result of the investigation is the comprehensive data set, which is available on a public server. This data can be used in a VPP to optimise downwind sailing in smooth water. Several interesting conclusions can also be drawn directly from the data. Thus, for the light wind case the best sheet angle is 90° regardless of the course sailed. However, for the strong wind case (dead downwind), the best angle is 80°. In all cases the tight kicker trim produces the largest drive force and in the light wind case also the smallest side force.

Keywords: ILCA 7; Downwind Sailing; Wind Tunnel; Scaling; FSI; Blockage; Sail Coefficients.

NOMENCLATURE

c_{CE}	Chord length at centre of effort [m]
C_F	Aerodynamic force coefficient [-]
C_M	Moment coefficient [-]
E	Young's modulus [GPa]
F	Aerodynamic force [N]
I	Area moment of inertia [m^4]
L	Characteristic length [m]
L_1	Length of bottom section [m]
L_2	Length of top section [m]
L_t	Total length of mast [m]
M	Moment [Nm]
P	Point load [N]
Re	Reynolds number [-]

r_{in}	Radius, inner [m]
r_{out}	Radius, outer [m]
S	Sail area [m^2]
t	Sail cloth thickness [m]
V	Wind speed [m s^{-1}]
V_{AW}	Apparent wind speed [m s^{-1}]
V_{mg}	Velocity made good [m s^{-1}]
x, y, z	Cartesian coordinates
y^+	Non-dimensional wall distance in wall functions [-]
α_E	Elastic scale factor [-]
α_F	Force scale factor [-]
α_I	Area moment of inertia scale factor [-]
α_L	Linear length scale factor [-]
α_P	Point load scale factor [-]
α_t	Thickness scale factor [-]
α_V	Velocity scale factor [-]
β_{AW}	Apparent wind angle [°]
δ	Sheet angle [°]
Δ_c	Length of cut in sail [m]
δ_1	Deflection of section 1 [m]
δ_2	Deflection of section 2 [m]
δ_t	Total deflection [m]
ε	Strain [m]
ν	Kinematic viscosity [m^2 s^{-1}]
ϕ	Heel angle [°]
ρ	Fluid density [kg m^{-3}]
σ	Tensile stress [Pa]
σ_{std}	Standard deviation [-]
θ	Deflection angle [°]
BRC	Balance Resolving Centre
CAD	Computer Aided Design
CE	Centre of Effort
CFD	Computational Fluid Dynamics
DOF	Degrees Of Freedom
FSI	Fluid-Structure Interaction
GKSS	Royal Gothenburg Yacht Club
ILCA	International Laser Class Association
LKT	Loose Kicker Trim
MKT	Medium Kicker Trim
ORC	Offshore Racing Congress
RANS	Reynolds-Averaged Navier-Stokes
RMS	Root Mean Square
SNIC	Swedish National Infrastructure for Computing
TKT	Tight Kicker Trim
VPP	Velocity Prediction Program

An index i indicates a vector component in either one of the three coordinate directions. Subscript p and m stand for prototype (full-scale) and model, respectively.

1 INTRODUCTION

Downwind racing is difficult, particularly in dinghies where the positioning of the crew plays a major role. The course should be optimised to give the maximum velocity made good (V_{mg}) towards the leeward mark, i.e. the increase in speed sailing closer to the wind has to be balanced by the larger distance sailed. There is an optimum heel angle of the dinghy. When it heels the centre of effort of the sail moves sidewards which creates a yaw moment that has to be balanced by the rudder. This may cause unnecessary resistance. To find the best sheet angle, not only the largest drive force should be considered. The side force is important since it will create an induced resistance of the underwater body. Kicker setting is another important parameter. A tight kicker bends the mast and increases the projected sail area. On the other hand, it also flattens the sail, which may make it less efficient downwind. To find the optimum configuration of all variables three components are required: an aerodynamic model, a hydrodynamic model, and a Velocity Prediction Program (VPP) linking the aerodynamic and hydrodynamic forces.

The primary objective of the present work is to increase the understanding of downwind sailing in dinghies, and in the present paper the first part of the investigation is reported. Detailed aerodynamic wind-tunnel data are presented for the Olympic ILCA 7 (formerly Laser Standard) dinghy (ILCA, 2023). Hydrodynamic data, as well as VPP-predictions will be presented in a future paper. All measured data will be made publicly available.

Although there is an extensive literature on sail aerodynamics there is very little data presented from wind-tunnel measurements where the trim of the sail is systematically varied. Sail trim optimisation is possible in real time in the most well-known wind-tunnels for sail studies, namely the one at the Technical University of Milan (Fossati, 2010) and the (now closed) tunnel at the University of Auckland (Le Pelley and Richards, 2011). There, the measured forces are input to a real-time VPP, and the sail trim is optimised for maximum V_{mg}. So, the sails are tested at optimum trim. Early sail trim data from the wind-tunnel at the Wolfson Unit (Wolfson Unit, 2023) are, however, presented by Marchaj (1979). He varied systematically the sheet angle and the kicker trim for a Finn dinghy. This was for upwind sailing. For downwind sailing the interest has mainly focused on spinnakers, where the role of the leading edge vortex has been investigated in a series of papers by Viola and co-workers (see e.g. Viola and Flay (2009); Viola and Flay (2010); Viola et al. (2014); Arrendondo-Galeana and Viola (2018) and Souppez et al. (2021)). The flow around a spinnaker is however fundamentally different from that on a mainsail at a large angle of attack. While the flow around a well-trimmed spinnaker separates at the leading edge and reattaches behind a separation bubble containing the leading edge vortex, the flow around a mainsail at large angles of attack is completely separated. This will be further discussed below. Note that for very fast hulls, like catamarans and foiling crafts, the angle of attack may be small enough for the flow to reattach, in spite of the effect of the mast. However, the present project concerns non-foiling dinghy monohulls.

There are good reasons to select the ILCA 7 as an example. It is one of the world's most popular dinghies, and it is an Olympic class for both men and women. This has prompted several academic studies, but mainly within hydrodynamics. Towing tank data for a half scale model were presented by Day and Nixon (2014) and towing tests of the full-scale Laser hull have been reported by Carrico (2005), Harrison (2012) and de-Meijer (2014). Towing tank tests at full-scale were carried out by Lindstrand and Peters (2014) at SSPA (now SSPA Maritime Center after becoming a part of RISE Research Institutes of Sweden), where the total resistance was measured for different boat speeds at varying heels and trims. Pennanen et al. (2016) continued the research on the ILCA dinghy and developed a tailor-made VPP for investigating upwind performance. This was used for predicting the optimum position of the sailor at different wind conditions. Lindstrand and Larsson (2017) used the ILCA 7 as an example in the development of a CFD-based VPP, where the interaction between the centerboard and rudder was investigated. Both VPPs used the ORC coefficients for the sail aerodynamics (ORC, 2021).

Aerodynamic data for the ILCA are very scarce. To the knowledge of the authors the only earlier investigation is that by Flay (1992). Special emphasis was on the oncoming flow. The velocity gradient due to the atmospheric boundary layer was considered as well as the ambient turbulence level. Two apparent wind angles were investigated: 30° and 60°. Downwind sailing was not considered, and no attention was paid to the Fluid-Structure Interaction (FSI), i.e. mast bend and sail cloth stretching.

There is thus need for aerodynamic data relevant to downwind sailing. FSI must be considered and systematic variations of important parameters such as apparent wind angle (course), sheet angle, heel angle and kicker trim should be included. In the present paper such data are presented, and a reference is given to a public data base, where all results can be retrieved.

2 THE ILCA 7 DINGHY

The ILCA dinghy was designed by Bruce Kirby in 1969 and the production started in 1970 under the name Laser. It is a strict one-design class, and it soon became very popular. More than 215 000 dinghies have been produced to date, and there are sailors in more than 120 countries. In 1996 the class became Olympic. However, due to a trademark dispute the name of the class was changed to ILCA in 2021. The dinghy comes with three rigs of different sizes, and in the present work the largest rig of 7.06 m^2 is investigated. This corresponds to the old Laser Standard and is used for men in the Olympics. The new name is ILCA 7.

The new MKII sail for the ILCA 7 is manufactured of 4.5 ounce Dacron cloth with a bi-radial design, which better matches the load paths and thus offers better durability than the old MKI sail, manufactured of 3.8 ounces Dacron and with a cross-cut design with diagonally placed panels. The MKII sail is also designed with a larger camber close to the mast, which will have an effect on the measured data presented below. The ILCA dinghy with the MKII sail can be seen in Fig. 1 and the main data for the sail is given in Tab. 1.

Figure 1. The ILCA 7 dinghy with the bi-radial MKII sail.

Table 1. MKII full-scale data.

Luff length (max) [m]	5.120
Leech length (max) [m]	5.555
Foot length (max) [m]	2.750
Sail area [m^2]	7.06

The mast for the ILCA 7 dinghy consists of a bottom section and a top section; it is combined by inserting the top section into the bottom section with an overlap (Fig. 2). The newest class-approved mast top section is produced in carbon composite, but in the present paper the traditional aluminum top section is considered together with the bottom section, also in aluminum.

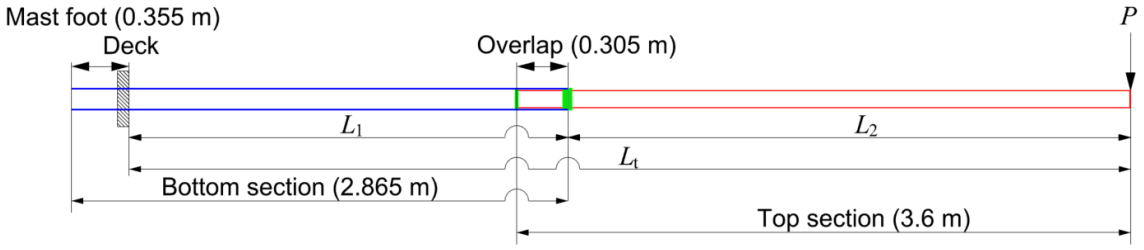

Figure 2. Illustration of the ILCA 7 mast, with the bottom and top sections. Note the length notation of the sections, which will be used in the following.

3 METHOD

In this Section the scaling of the sail and mast is discussed first, followed by a description of the experimental setup.

3.1 Scaling

As in all model testing, geometric similarity between model and prototype (full-scale) is imperative. In sail aerodynamics, this means that both the sail stretching and the mast bend must be scaled correctly. This is particularly important for the unstayed mast of the ILCA 7 because the large mast bend will have a profound impact on the shape of the sail. For the flow to be scaled correctly both kinematic and dynamic similarity are required. Force coefficients are then unchanged between the scales. See Larsson and Raven (2010) for an introduction to the concepts. In most wind-tunnel testing dynamic and kinematic similarity is achieved if the ratio between the inertial and viscous forces is the same at the two scales. This condition is satisfied if the Reynolds number is constant. The Reynolds number is defined as

$$Re = \frac{V L}{\nu}, \tag{1}$$

where V is the wind speed, L is a characteristic length and ν is the kinematic viscosity. However, in the testing of very thin membranes, such as spinnakers, gravity also has to be considered. As is well known, a spinnaker may change shape considerably, and even collapse in very light airs. The ratio between inertial and gravity forces may be expressed by a Froude number (Viola, 2013), and in theory this has to be constant between the scales. However, gravity has a much smaller effect on a mainsail, which is much stiffer, and supported by the mast and boom. In the present tests the gravity effect is neglected.

Constant force coefficients yield the following relation between corresponding forces at the two scales

$$\frac{F_p}{F_m} = \frac{\rho_p}{\rho_m}\left(\frac{V_p}{V_m}\right)^2\left(\frac{L_p}{L_m}\right)^2, \tag{2}$$

where F represents the aerodynamic force and ρ the fluid density. The indices p and m stand for prototype (full-scale) and model, respectively. Representing the ratio of model scale and prototype scale quantities by α, this relation may be written

$$\alpha_F = \alpha_V^2\,\alpha_L^2, \tag{3}$$

where the same density is assumed at the two scales.

3.1.1 Sailcloth Stretching

Correct scaling of deformations between the two scales implies constant strain, ε (dimensionless deformation)

$$\varepsilon_m = \varepsilon_p. \tag{4}$$

But according to Hooke's law

$$\sigma = E\,\varepsilon, \tag{5}$$

where σ is the stress and E is Young's modulus. The stress at any cut of length Δ_c through the sail is

$$\sigma = \frac{F}{\Delta_c\,t}, \tag{6}$$

where F is the normal force on the cut and t is the cloth thickness. From Eq. 5 & Eq. 6

$$\varepsilon = \frac{F}{E\,\Delta_c}\,t. \tag{7}$$

With the appropriate scale factors introduced, this yields for the model

$$\varepsilon_m = \frac{F_m}{E_m\,\Delta_{c_m}\,t_m} = \frac{\alpha_F\,F_p}{\alpha_E\,E_p\,\alpha_L\,\Delta_{c_p}\,\alpha_t\,t_p}. \tag{8}$$

Using Eq. 3 & Eq. 4, this yields

$$\frac{\alpha_V^2\,\alpha_L}{\alpha_E\,\alpha_t} = 1. \tag{9}$$

This condition is satisfied for $\alpha_L = 1/7$, $\alpha_V = \sqrt{7}$, $\alpha_E = 1$ and $\alpha_t = 1$. Thus, scaling the velocity by the factor $\sqrt{7}$, the $1/7$-th model sail will have the same dimensionless deformation as the prototype with the same sail cloth ($\alpha_E = 1$ and $\alpha_t = 1$).

3.1.2 Mast Bend

To scale the bending, the mast is assumed composed of two sections, the bottom one, of length L_1, from the deck level to the upper end of the overlap, and the top one, of length L_2, from the overlap to the top. The bottom section is assumed clamped at the deck level and the total length of the mast is L_t, see Fig. 2.

A free-body diagram is shown in Fig. 3, assuming a point load P at the top of the mast. The effect of the increased stiffness in the overlap is thus neglected.

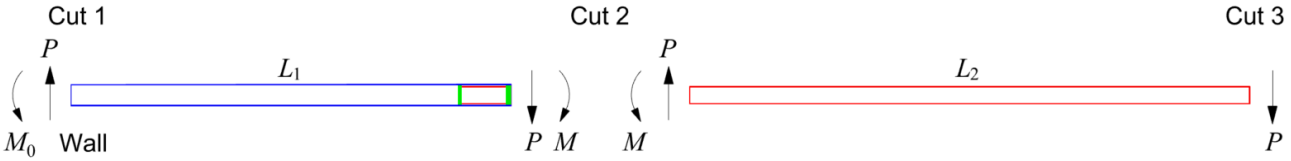

Figure 3. Free body diagram of the ILCA 7 mast, presented in Fig. 2.

The total deflection at the top of the mast, δ_{top} may be obtained as

$$\delta_{top} = \delta_1 + \delta_2 + L_2 \sin\theta, \tag{10}$$

where δ_1 and δ_2 are the deflections of sections 1 and 2, respectively and θ is the deflection angle at cut 2. For small angles sin(θ) may be replaced by θ in radians.

According to elementary beam theory (Beer et al., 2012), the deflection δ of a cantilever beam in pure bending exposed to a concentrated (point) load P and moment M at the free end is obtained from

$$\delta = \frac{P\,L^3}{3\,E\,I} + \frac{M\,L^2}{2\,E\,I}, \tag{11}$$

and the deflection angle from

$$\theta = \frac{P\,L^2}{2\,E\,I} + \frac{M\,L}{E\,I}, \tag{12}$$

where I is the area moment of inertia.

Since

$$M = P\,L_2, \tag{13}$$

the three terms of Eq. 10 may be written

$$\delta_1 = \frac{P\,L_1^3}{3\,E\,I} + \frac{P\,L_2\,L_1^2}{2\,E\,I} = \frac{P\,L_t^3}{E\,I}\left[\frac{1}{3}\left(\frac{L_1}{L_t}\right)^3 + \frac{1}{2}\left(\frac{L_1}{L_t}\right)^2\frac{L_2}{L_t}\right], \tag{14}$$

$$\delta_2 = \frac{P\,L_2^3}{3\,E\,I} = \frac{P\,L_t^3}{E\,I}\left[\frac{1}{3}\left(\frac{L_2}{L_t}\right)^3\right], \tag{15}$$

$$L_2\,\theta = \frac{P\,L_1^2\,L_2}{2\,E\,I} + \frac{P\,L_2^2\,L_1}{E\,I} = \frac{P\,L_t^3}{E\,I}\left[\frac{1}{2}\left(\frac{L_1}{L_t}\right)^2\frac{L_2}{L_t} + \frac{L_1}{L_t}\left(\frac{L_2}{L_t}\right)^2\right]. \tag{16}$$

Thus, all three terms are proportional to $P\,L_t^3/E\,I$ and all quantities within the square brackets are length fractions, L_1/L_t or L_2/L_t, which are unchanged between the two scales.

Dividing all terms by L_t to get the dimensionless deflection, all terms will be proportional to $P\,L_t^2/E\,I$.

But

$$\left(\frac{P\,L_t^2}{E\,I}\right)_m = \frac{\alpha_P\,\alpha_L^2}{\alpha_E\,\alpha_I}\left(\frac{P\,L_t^2}{E\,I}\right)_p, \tag{17}$$

and the point load P scales as the distributed force F in Eq. 3, i.e.

$$\alpha_P = \alpha_V^2\,\alpha_L^2. \tag{18}$$

Thus, for all three components of the mast deflection to scale properly the following relation must hold:

$$\frac{\alpha_V^2\,\alpha_L^4}{\alpha_E\,\alpha_I} = 1. \tag{19}$$

Inserting the scale factors for wind speed and length, $\alpha_V = \sqrt{7}$ and $\alpha_L = 1/7$ the following relation is obtained

$$\alpha_E\,\alpha_I = 2.92 \times 10^{-3}. \tag{20}$$

That is:

$$\frac{I_m}{I_p} = 2.92 \times 10^{-3} \frac{E_p}{E_m}. \tag{21}$$

To scale the mast as well as possible geometrically, the mast model was made up of a stainless steel rod with a Young's modulus of 196 GPa. For the prototype aluminum mast, Young's modulus is 60 GPa. Inserting these numbers in Eq. 21 above, a relation between the area moments of inertia of the model and prototype is obtained

$$I_m = 0.894 \times 10^{-3} I_p. \tag{22}$$

The prototype mast is made of circular tubes, for which the area moment of inertia may be written:

$$I_p = \frac{\pi}{4} \left(r_{\text{out}}^4 - r_{\text{in}}^4 \right), \tag{23}$$

where r_{out} and r_{in} are the outer and inner radii, respectively. For the model mast rod, the area moment of inertia is related to the radius as follows

$$I_m = \frac{\pi r_m^4}{4}. \tag{24}$$

Solving for the radius:

$$r_m = \left(\frac{4 I_m}{\pi} \right)^{1/4}, \tag{25}$$

with I_p from Eq. 23, I_m can be obtained from Eq. 22, which yields the radius of the model mast rod in Eq. 25. Note that these relations hold for both sections of the mast. The result is presented in Tab. 2.

Table 2. Inner and outer radii and area moment of inertia for each part of the prototype mast; radius and area moment of inertia for each part of the model mast.

	Prototype, $E = 60\,\text{GPa}$			**Model**, $E = 196\,\text{GPa}$	
Section	$r_{\text{out}} \times 10^3$ [m]	$r_{\text{in}} \times 10^3$ [m]	$I_p \times 10^6$ [m^4]	$r \times 10^3$ [m]	$I_m \times 10^6$ [m^4]
Bottom	31.75	28.75	0.261	4.15	0.233
Top	25.60	23.60	0.0941	3.20	0.0841

3.1.3 Scale Effects

While it was possible to correctly scale the sail stretching by proper scaling of the wind speed ($\alpha_V = \sqrt{7}$) for the chosen geometric scale ($\alpha_L = 1/7$), it was not possible to exactly scale the mast diameters. However, by the choice of stainless-steel for the model mast, the scale factor for the bottom section was $1/7.7$ and for the top section 1/8. So, the model mast was slightly thinner than a correctly scaled mast. This small difference is neglected in the following. In the derivations above it has been assumed that the Reynolds number is the same in the two scales. This is not true, since the velocity is increased by a factor $\sqrt{7}$, while the linear dimension is decreased by a factor 7 for the model. So, assuming the same kinematic viscosity, the model scale Reynolds number is $\sqrt{7}$ times smaller than in reality. For the light wind case the Reynolds numbers were 181 000 and 477 000 at model and full scale, respectively, while the corresponding numbers in the strong wind case were 303 000 and 803 000. These differences are also neglected. The flow around the downwind sail is dominated by massive separation at the fixed edges of the sail, so the location of separation is unchanged between the scales. This means that the forces coefficients are practically independent of Reynolds number. See e.g. Hoerner (1965) who shows that the drag of a flat plate at right angles to the flow is independent

of Reynolds number over the range 10^4 to 10^7.

A picture of the flow around the ILCA 7 sail at the center of effort level is shown in Fig. 4. This is from the CFD computations of the blockage presented below. Note that this is a very different flow field compared to that of a well-trimmed spinnaker, where a separation bubble is created at the leading edge of the suction side and the reattached flow separates a second time on the curved surface of the sail further downstream. The downstream separation point is critically dependent on the Reynolds number, as this determines whether the reattached boundary layer is laminar or turbulent. See e.g. Souppez et al. (2021). There is no such effect in the present case, as the flow never reattaches on the suction side.

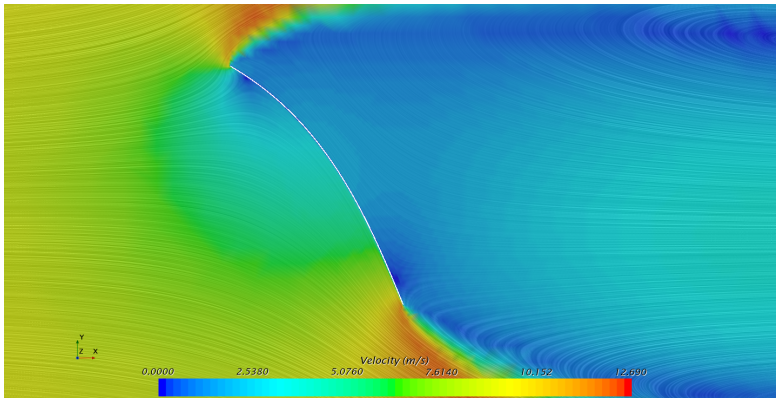

Figure 4. Time averaged top view of the flow around the ILCA 7 sail, at the center of effort level in the large computational domain. Streamlines and velocity magnitude at 60° angle of attack, upright. The undisturbed flow is in the positive x direction.

3.2 Experimental Setup

3.2.1 Chalmers' Low-Speed Wind Tunnel

Chalmers' subsonic wind tunnel is a classic closed loop tunnel that operates at atmospheric pressure. An external 6-DOF strain-gauge wind tunnel balance was used to measure the forces and moments. In Fig. 5 an upwind view of the octagonal-shaped test section can be seen. The length of the test section is 3.0 m and the sail was centrally positioned 1.5 m downstream of the inlet, which has a cross-sectional area of 2.07 m^2 (1.8 $\times$ 1.2 m^2 minus the corner fillets). The tunnel had no means for simulating the atmospheric boundary layer, but a grid that produced a turbulence intensity of 2% was used.

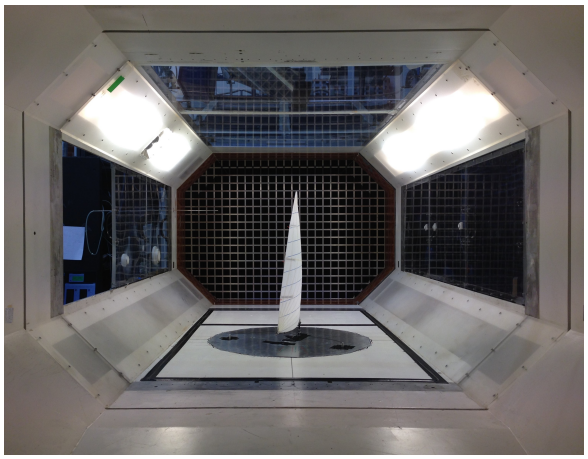

Figure 5. Upwind view of the octagonal test section, seen from the diffuser. Note the grid at the inlet.

3.2.2 Test Matrix

The test matrix for the light wind case, consisted of altogether 315 configurations (illustrated in Fig. 6) where 5 apparent wind angles (β_{AW}), 7 sheet angles (δ), 3 heel angles (ϕ) and 3 kicker trims, loose (LKT), medium (MKT) and tight (TKT), were tested. The test matrix for the strong wind was limited to only 12 configurations dead downwind (180°) at zero heel. In this sailing mode, the sheet angle should be no larger than 90°, so only the four angles between 60° - 90° were tested. For each sheet angle, there were three kicker settings.

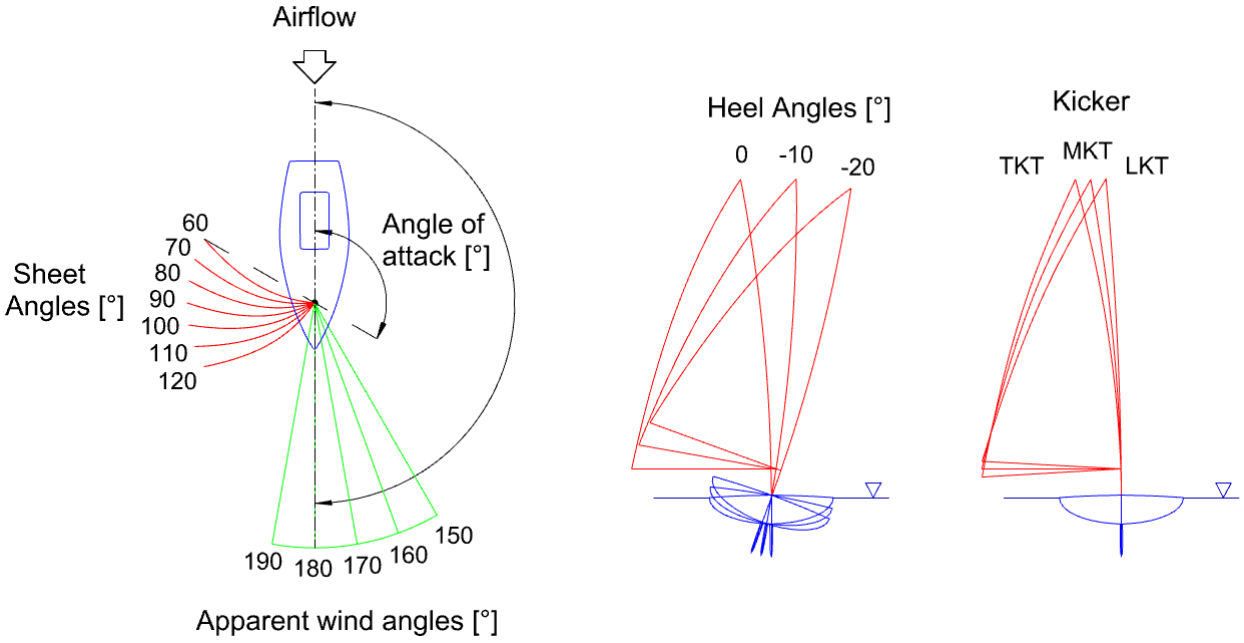

Figure 6. Illustrations of the test matrix showing the sheet angles (δ) and apparent wind angles (β_{AW}) in a top view; the heel angles (ϕ) and the kicker settings in an upwind view.

3.2.3 Coordinate System

The coordinate system is defined in Fig. 7. It has its origin in the intersection between the undisturbed water surface and the centre plane at the longitudinal position of the mast. x is forwards, y horizontally to port and z vertically upwards. Note that positive rotation in roll is to starboard. Since the boat heeled to port in the experiments all heel angles are negative. F_x, F_y and F_z are the aerodynamic drive force, side force and lift force, respectively and M_x, M_y and M_z are the roll, pitch and yaw moments, respectively.

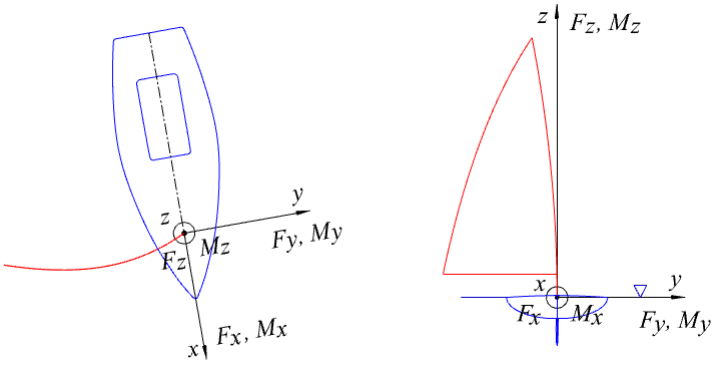

Figure 7. Illustrations of the coordinate system.

3.2.4 Trimming the Sail

The ILCA dinghy has four trim controls, i.e. sheet, kicker, Cunningham and outhaul, see Fig.8. All these were used to trim the sail model, but in the tests, the sheet and the kicker were decoupled. The kicker was positioned further aft, and took over the function of flattening the sail by pulling the boom downwards from the sheet, which in the tests only controlled the sheet angle. The Cunningham and the outhaul were positioned as on the full-scale ILCA dinghy and controlled the luff and the foot tensions of the sail, respectively.

To test the sail for the three different heel angles, a mounting bracket with a separate mast foot for each heel angle was used (see Fig. 8 and Fig. 9), where the top surface of each mast feet represented the deck surface of the ILCA dinghy. The sail was trimmed manually by pulling thin, static, and strong ropes, that ran from their attachment-points on the sail/boom, through blocks and through the mounting bracket, to the keyboard where they were attached to horn- and clam cleats, as illustrated in Fig. 8. To set the boom at the desired sheet angle, markings, which represented the sheet angles, were printed on the wind tunnel floor, corresponding to the calm water surface in the tests.

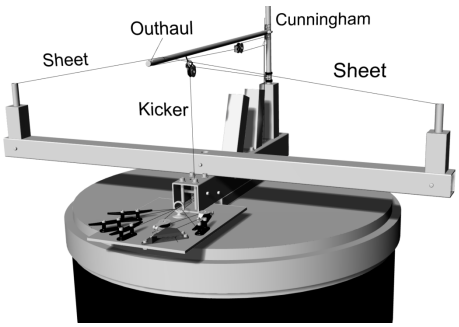

Figure 8. A CAD model of the external wind tunnel balance, the mounting bracket and the different trim controls. Note that the sheet only controls the sheet angle and that the kicker, which is mounted further aft controls the flattening of the sail.

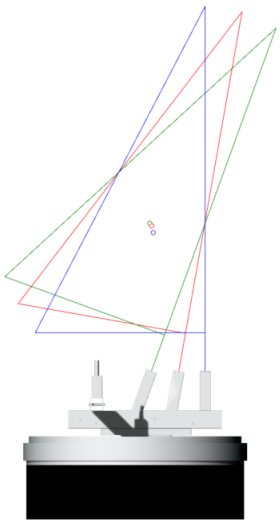

Figure 9. Illustration, seen upwind, of the mast and sail mounted in the three different mast feet, representing (from left to right) the three heel angles -20°, -10° and 0°.

Fig. 10 - 12 shows three pictures of the sail, with -20° heel angle and 90° sheet angle, being tested for the three different kicker settings. The loose kicker trim Fig. 10 corresponds to a slight pull of the kicker, the tight kicker trim Fig. 12 corresponds to a hard pull that gave some wrinkles in the sail and the medium kicker trim Fig. 11 corresponds to a setting between the loose and the tight kicker trim.

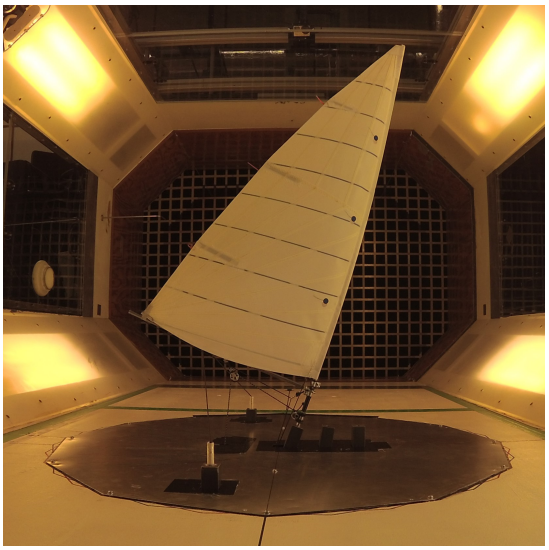

Figure 10. Loose kicker trim (LKT).

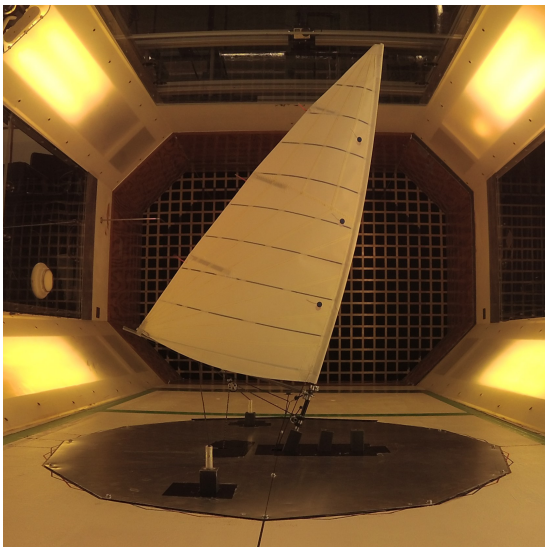

Figure 11. Medium kicker trim (MKT).

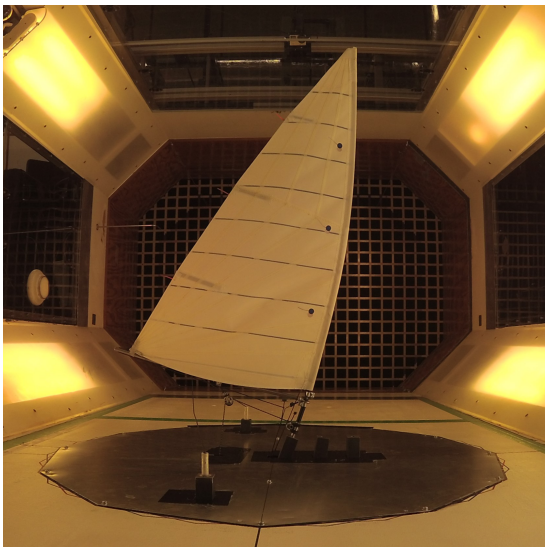

Figure 12. Tight kicker trim (TKT).

The range of kicker trims was found after consulting elite ILCA 7 sailors from the Royal Gothenburg Yacht Club (GKSS), who attended some of the tests. Instructions on how to adjust the Cunningham and outhaul for optimum performance were also provided. The slack from the Cunningham was pulled slightly and kept relatively loose for all tests while the outhaul was continuously adjusted (for both wind speeds) to obtain the best camber of the sail. This procedure introduces some arbitrariness in the tests, but the only other alternative would have been to include the Cunningham and the outhaul in the list of variables, which would have increased the test matrix beyond possible limits. It is thus inherently assumed in the results that the two variables were set at their optimum values in all tests.

3.2.5 Test Procedure

To set the speed for the strong wind case a speed test was carried out, where the sail, the mast and the other equipment were tested for a model-scale apparent wind speed of 18.5 m s^{-1}. This speed corresponds to a full-scale apparent wind speed of 7 m s^{-1}, and is a planing speed for the ILCA dinghy. The speed test showed no risk for structural damage neither to the sail, mast or the other equipment, nor to the load-cells, so this speed was chosen for the strong wind case. The speed for the light wind case was chosen with the accuracy of the balance in mind, and to avoid too small forces, a model-scale apparent wind speed of 10.6 m s^{-1} was chosen. This corresponds to a full-scale apparent wind speed of 4 m s^{-1}.

The sampling frequency was 1 kHz and each test was run for 30 seconds. Every second a mean value was computed. The final result was obtained as the root mean square (RMS) of the mean values.

To be able to correct the measurements for non-zero initial sampling values and check how often it was necessary to reset the balance to zero, zero-samplings were taken before every new sheet angle when the balance was unloaded and the circulating airflow had calmed down. If the difference between the two zero-samples was larger than 3% the balance was reset to zero and the particular test case was repeated. A detailed description of the test procedure is given in Magnander (2022). To also correct the measurements for drag tare, caused by the mounting-bracket that protruded the wind tunnel floor, and the other small equipment, drag tare tests were carried out for both apparent wind speeds.

After all wind tunnel tests were finished the balance was moved into a calibration frame and balance tests were performed. The balance measurement errors of the forces and moments were found to be 0.3-1.2% in five DOFs. (The sixth DOF, vertical lift, was very small and is of less interest in the investigation).

To get a measure of the precision error, repeatability tests were carried out. It was regarded sufficient to only perform these tests for one of the apparent wind speeds (V_{AW}) and one apparent wind angle (β_{AW}), and since the repeatability tests were carried out directly after the light wind tests with the apparent wind angle 190°, the same apparent wind speed, and the same apparent wind angle were chosen for all repeatability tests. The sheet angle was 90° and all three heel angles and kicker trims were tested. For each configuration five repetitions were made. In Fig. 13 the standard deviation (σ_{std}) of each configuration for the drive force coefficients can be seen. The average value of all configurations is 2.9%; can be assumed to also hold for the other components.

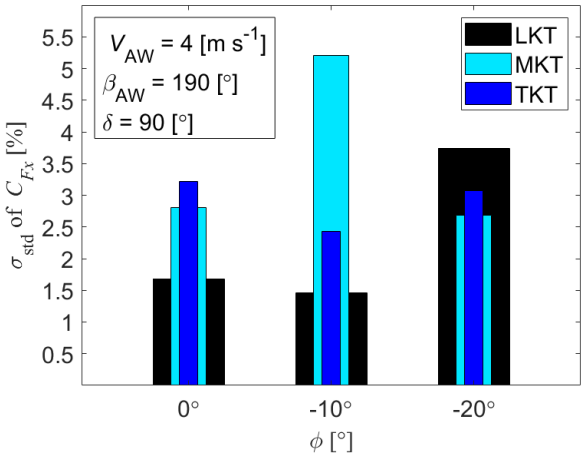

Figure 13. Standard deviation (σ_{std}) of the drive force coefficients (C_{F_x}).

3.2.6 Post-Processing

The measurements were corrected for non-zero initial sampling values, drag tare, balance measurement errors and also for blockage effects. How the measurements were corrected for blockage is described in the following section.

Measured forces and moments were obtained in a coordinate system with its origin at the balance resolving centre (BRC). The coordinate axes were aligned with the x, y, z-axes defined in Fig. 7, but the origin was different. Since forces and moments are presented in the x, y, z-system a transformation of the moments were made. Also, a correction was made for the lateral displacement of the mast feet relative to the origin (see Fig. 9).

3.2.7 Blockage Effects and CFD

Due to the test section boundaries in Chalmers' wind tunnel, blockage effects must be considered and the measurements corrected. With a sail area of 0.144 m^2 and a wind tunnel cross-sectional area of 2.07 m^2 the maximum blockage ratio was 7.0%. If the test object has a streamlined geometry, like a wing profile, standard formulas (Barlow et al., 1999) can be used, but if the test object is not streamlined like a relatively flat sail, more or less perpendicular to the airflow in downwind sailing, these formulas cannot be used. Therefore a comprehensive numerical investigation of the blockage was carried out.

The commercial flow solver STAR-CCM+ was used for solving the Reynolds-Averaged Navier-Stokes (RANS) equations. Two computational domains of different sizes were used. One with the same cross-sectional area as the test section, and the other 4 times larger. The blockage ratio for the larger domain was thus $7/4 = 1.75\%$, which was considered small enough for blockage effects to be neglected (see e.g. Souppez and Viola (2022)). The results from this domain may thus be considered unaffected by the tunnel walls and the difference in results between the domains a measure of the blockage effects. Therefore, measured force and moment coefficients were corrected by the ratio of the values obtained in the large and small domains respectively. The length of the domains was $30\,L$ and the position of the sail, downstream of the inlet, was $10\,L$. For the inlet and outlet boundaries, the "velocity inlet" and "pressure outlet" types were used, respectively. Slip boundary conditions were applied for the lateral boundaries, while a no-slip condition with the two-layer all y^+ wall treatment function was used for the sail. The ambient turbulence was set to the measured value: 2%.

Several turbulence models were tested, but the final computations were carried out using the realizable $k-\varepsilon$ two-layer model. Verification was made using five grids for the light wind case with an apparent wind angle of 180°, a sheet angle of $90°$, upright and with a tight kicker setting. The es-

timated uncertainties (from Eca and Hoekstra (2014)) for the grids used in the blockage correction were 3.6% and 4.1% for the ”normal” and ”large domains”, respectively.

No formal validation was carried out, but the difference (comparison error) between computed and measured values for the normal domain was relatively large, typically 10% for the drive force. Since this is considerably larger than the numerical uncertainty, it must be due to modeling errors. A likely reason for these errors is the steady state assumption in the RANS computations which may be inaccurate in the wake of the sail. As the results were used for computing a relatively small correction, the accuracy should be acceptable. The CAD model of the sail was modeled with a tight kicker trim, because the tests showed that this kicker setting gave highest drive force coefficients overall. Only the dead downwind and upright sailing condition was simulated, but simulations for all seven sheet angles were performed.

Fig. 14 & Fig. 15 below, show plots with correction factors calculated with the drive force coefficients and side force coefficients from the RANS simulations and extrapolated correction factors for the sheet angles: 50°, 130°, 140° and 150°.

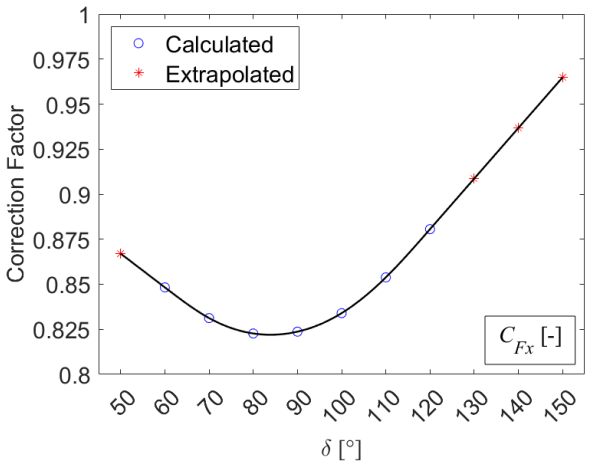

Figure 14. Calculated and extrapolated correction factor for the drive force coefficient (C_{F_x}) vs sheet angle (δ). The extrapolation was done with cubic splines.

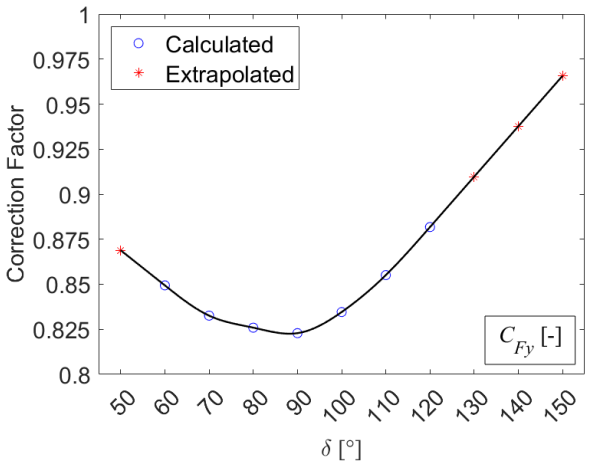

Figure 15. Calculated and extrapolated correction factor for the side force coefficient (C_{F_y}) vs sheet angle (δ). The extrapolation was done with cubic splines.

The correction factor for the drive force was also used to correct the pitch and yaw moments, while the correction factor for the side force was also used to correct the roll moment. The lift force was not corrected for blockage, because its magnitude is so small that it is of no significant interest.

4 RESULTS AND DISCUSSION

The major objective of the present paper is to introduce a data set for the aerodynamics of the ILCA 7 sailing downwind. This data set is publicly available at the EU-funded database (Zenodo, 2023), together with the MSc. report (Magnander, 2022) which describes the project in detail, including the comprehensive CFD investigation to determine the blockage effect. With the aerodynamic data set and the hydrodynamic data set from the towing tank tests (Lindstrand and Peters, 2014), a very accurate prediction of downwind sailing can be made using a VPP, without assumptions for the fluid dynamics.

In the data set, forces and moments are reported as coefficients, where all force coefficients, C_{F_i} are obtained from the force, F_i as follows:

$$C_{F_i} = \frac{F_i}{0.5\,\rho\,V^2\,S}, \tag{26}$$

where ρ is the air density, V the wind speed, S the sail area and the index i stands for one of the coordinate directions x, y or z, defined in Fig. 7. Moment coefficients C_{M_i} are given by:

$$C_{M_i} = \frac{M_i}{0.5\,\rho\,V^2\,S\,c_{\mathrm{CE}}}, \tag{27}$$

where $c_{\mathrm{CE}} = 0.250$ m is the chord length at the height of the geometrical CE in the sail model. In the following, F_x is called the drive force and F_y side force. M_z, the moment around the z-axis, is called yaw moment.

4.1 Light Wind Case

As appears from the test matrix, the data set from the wind-tunnel experiments is very large, so only a few typical examples can be presented here. For the light wind case (corresponding to a full-scale apparent wind speed of 4 m s^{-1}), drive force coefficients will be shown for the smallest, middle and largest apparent wind angles (β_{AW}), i.e. 150°, 170° and 190°, respectively, and only at zero heel. Side force coefficients will be presented for the same cases, while yaw moment coefficients will be given only for 170°, but at all three heel angles. This is because heel is the main parameter for determining the yaw moment. The remaining three coefficients are considered less important since both heel and pitch can be adjusted by the sailor position, and the heave effect is so small that it is of no practical importance.

4.1.1 Drive Force Coefficients

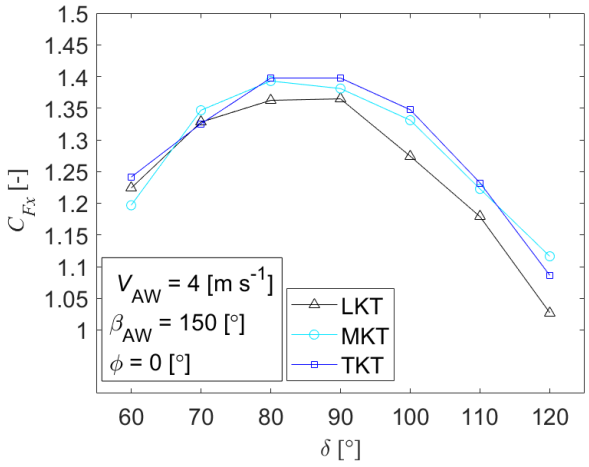

Figure 16. Drive force coefficient (C_{F_x}) vs sheet angle (δ) for the three kicker settings, the heel angle (ϕ) 0° and the apparent wind angle (β_{AW}) 150°.

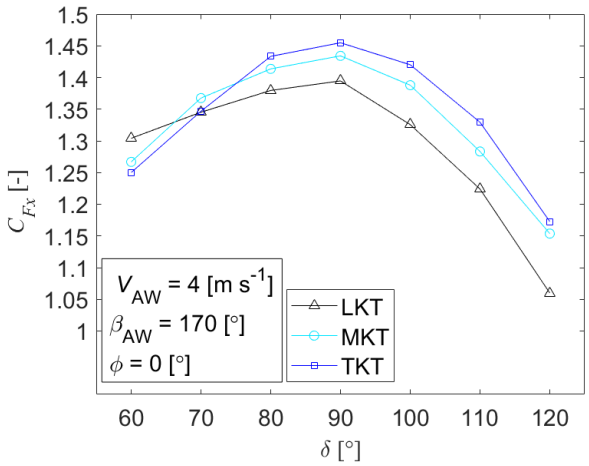

Figure 17. Drive force coefficient (C_{F_x}) vs sheet angle (δ) for the three kicker settings, the heel angle (ϕ) 0° and the apparent wind angle (β_{AW}) 170°.

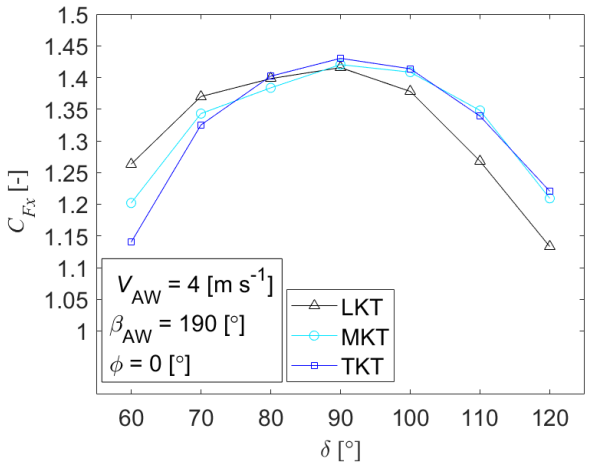

Figure 18. Drive force coefficient (C_{F_x}) vs sheet angle (δ) for the three kicker settings, the heel angle (ϕ) 0° and the apparent wind angle (β_{AW}) 190°.

Fig. 16 - Fig. 18 show the drive coefficient for the three apparent wind angles at zero heel. The drive force coefficient is shown as function of the sheet angle, and the three curves represent the different kicker settings. The general shape of all curves is quite similar: there is a rather distinct maximum and significant drops for too large or too small sheet angles.

Several conclusions may be drawn from the figures, but to get the full picture VPP computations are required. First, the maximum drive force at all apparent wind angles is obtained with the tightest kicker setting. Apparently, this is the setting with the largest mast bend (see Fig. 12) and thus the largest projected area normal to the boom. This advantage seems to be larger than the disadvantage of a flatter sail downwind.

Another important feature of the curves is that all maxima occur at 90° of sheet angle (except for the medium kicker setting at 150° apparent wind angle, where it is 80°). This would be expected dead downwind, i.e. at 180° apparent wind angle, where this sheet angle would yield the largest projected sail area in the direction of motion, but not at 150°. Here the largest projected area would be obtained at 60° of sheet angle. This indicates that the sail in this case works in a different way, compared to dead downwind, where it acts like a parachute. At 150° apparent wind angle the flow may be less separated and the sail working more like a wing.

Among ILCA 7 sailors there is a technique known as “sailing negative”, which means that the sail is

sheeted such that the flow moves from the trailing edge towards the leading edge. The angle of attack is thus larger than 90°. This is sometimes utilized downwind. There is, however, very little support for this in the data for the light wind case. With 90° of sheet angle, negative sailing would occur only for larger apparent wind angles than 180°. However, the maximum drive force coefficient for 190° is lower than for 170°. They are equally distant from dead downwind and would have the same apparent wind, as well as distance sailed.

4.1.2 Side Force Coefficients

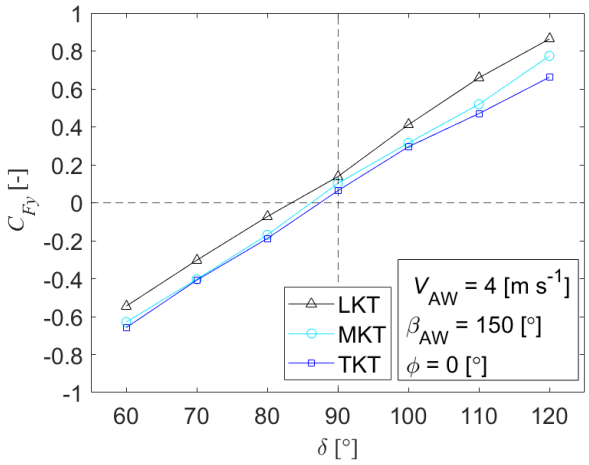

Figure 19. Side force coefficient (C_{F_y}) vs sheet angle (δ) for the three kicker settings, the heel angle (ϕ) 0° and the apparent wind angle (β_{AW}) 150°.

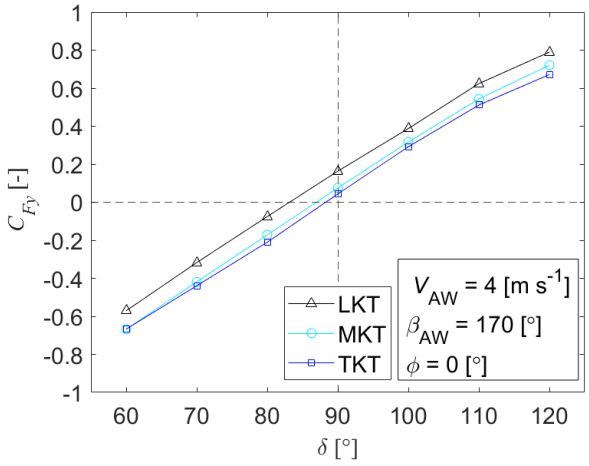

Figure 20. Side force coefficient (C_{F_y}) vs sheet angle (δ) for the three kicker settings, the heel angle (ϕ) 0° and the apparent wind angle (β_{AW}) 170°.

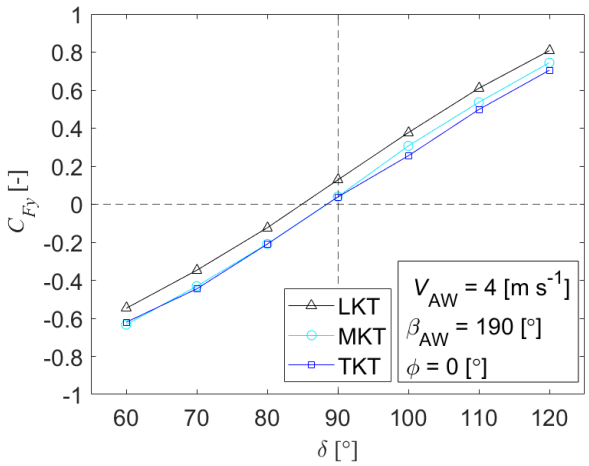

Figure 21. Side force coefficient (C_{F_y}) vs sheet angle (δ) for the three kicker settings, the heel angle (ϕ) 0° and the apparent wind angle (β_{AW}) 190°.

In Fig. 19 - Fig. 21 the side force coefficient for the same apparent wind angles is presented. There is an almost linear variation of the side force with sheet angle. Negative coefficients represent forces to leeward and positive to windward. First, it may be noted that the side force is always positive at 90 degrees of sheet angle, where the drive force is the largest. For courses close to dead downwind, where the sail acts like parachute, this is caused by the asymmetry of the sail cross-section around mid-chord. The flow from the stagnation point on the sail towards the mast experiences much larger curvature of the sail than the flow moving towards the leech, where the sail is almost flat. Further, there is the effect of the mast. The disturbance of the flow towards the mast is thus larger than that of the flow moving towards the leech, and thereby the total force will be turned to windward. For smaller apparent wind angles the sail acts more like a wing, and the lift will turn the resulting force to windward.

Another interesting feature of the figures is the consistent difference between the three kicker settings. The looser the kicker trim the larger (more positive) the side force. This is in line with the previous explanation: the looser the kicker, the larger the camber close to the mast. And thus, the larger the asymmetry effect just explained. Obviously, the side force should be kept as small as possible, since it will have to be balanced by the opposite force on the underwater body, generating an induced resistance. So, based on these diagrams only, the best sheet angle is slightly smaller than 90°. But the total optimum can only be obtained in a VPP. There is no support, however, for the significantly smaller sheet angles in negative sailing.

4.1.3 Yaw Moment Coefficients

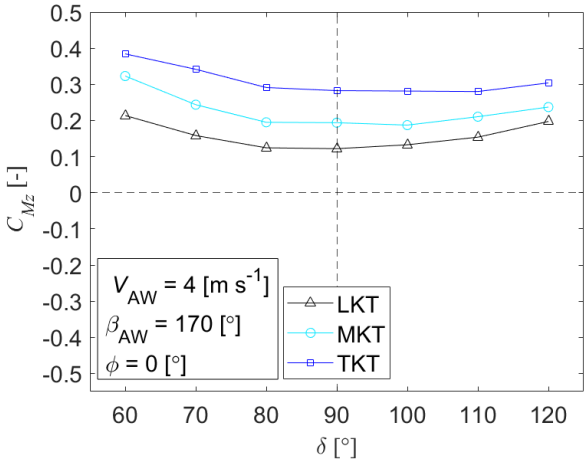

Figure 22. Yaw moment coefficient (C_{M_z}) vs sheet angle (δ) for the three kicker settings, the apparent wind angle (β_{AW}) 170° and the heel angle (ϕ) 0°.

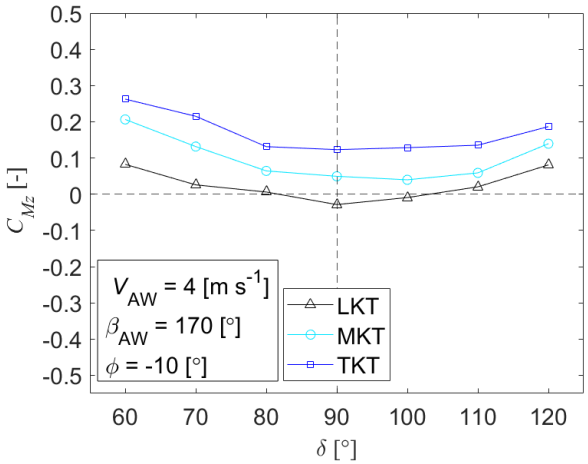

Figure 23. Yaw moment coefficient (C_{M_z}) vs sheet angle (δ) for the three kicker settings, the apparent wind angle (β_{AW}) 170° and the heel angle (ϕ) -10°.

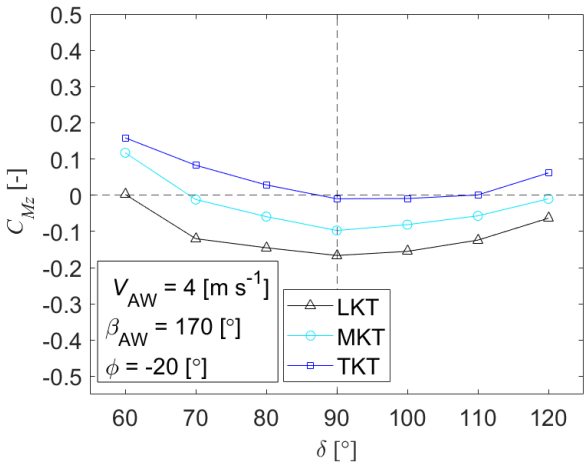

Figure 24. Yaw moment coefficient (C_{M_z}) vs sheet angle (δ) for the three kicker settings, the apparent wind angle (β_{AW}) 170° and the heel angle (ϕ) -20°.

The total yaw moment on the dinghy is created by the aerodynamic and hydrodynamic force couple in the horizontal plane. This moment should be minimised to avoid unnecessarily large rudder angles to balance the moment. A too large rudder angle will generate unnecessary induced resistance. To minimise the rudder angle both the aerodynamic and hydrodynamic forces need to be considered and this can only be done using a VPP. However, since the hydrodynamic force is likely to generate a small yaw moment, a small moment from the aerodynamics should be preferable.

In Fig. 22 - Fig. 24 the aerodynamic yaw moment coefficient is plotted against sheet angle for the three heel angles at the apparent wind angle 170°. Note that positive heel is to leeward. In general, the coefficient is reduced with heel. This is to be expected, since the centre of effort of the sail then moves closer to $y = 0$ (see the definition of the coordinate system in Fig. 7), in which the drive force generates no yaw moment. For all curves there is a minimum near 90° of sheet angle, where we have the largest drive force. There is a very interesting systematic difference between the kicker trims, where the yaw moment (to windward) increases when tightening the kicker. This is since the aerodynamic centre moves towards the leech when the mast is bent. It thus seems possible to minimise the yaw moment at all heels: a loose kicker trim at zero heel and at -10° of heel and a tight kicker trim at -20°. But, as mentioned above, the optimum heel and kicker trim can be obtained only by a VPP.

4.2 Strong Wind Case

4.2.1 Drive Force, Side Force and Yaw Moment Coefficients

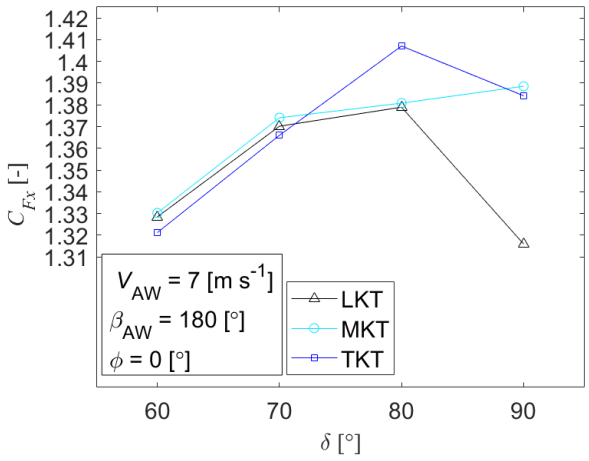

Figure 25. Drive force coefficient (C_{F_x}) vs sheet angle (δ) for the three kicker settings, the heel angle (ϕ) 0° and the apparent wind angle (β_{AW}) 180°.

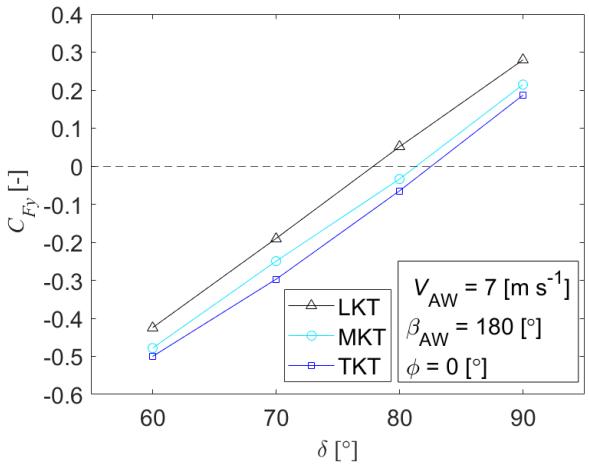

Figure 26. Side force coefficient (C_{F_y}) vs sheet angle (δ) for the three kicker settings, the heel angle (ϕ) 0° and the apparent wind angle (β_{AW}) 180°.

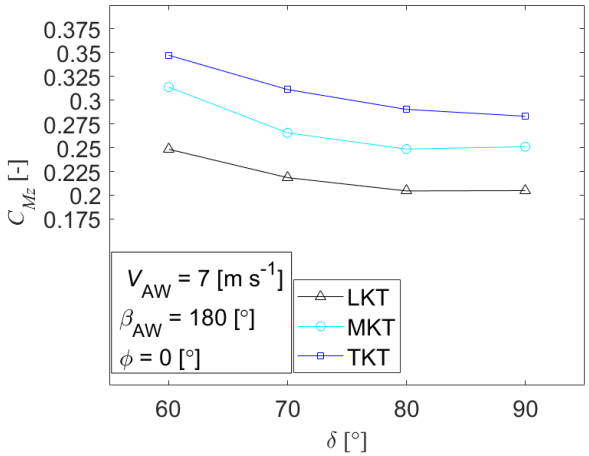

Figure 27. Yaw moment coefficient (C_{M_z}) vs sheet angle (δ) for the three kicker settings, the heel angle (ϕ) 0° and the apparent wind angle (β_{AW}) 180°.

For the strong wind case (corresponding to an apparent wind speed of 7 m s^{-1}) the measurements were limited to dead downwind (apparent wind angle 180°) and zero heel. Results for the three coefficients discussed for the light wind case are presented in Fig. 25 - Fig. 27. The graphs for the drive force are somewhat contradictory, since the curve of the medium kicker trim does not follow the trend of the two other trims, and there is no distinct maximum, like in all drive force curves for the light wind. Most likely, the last point on the curve is in error. With this caveat, the maximum drive force is now shifted to 80° sheet angle. This is an interesting observation, since it means that the maximum force is not obtained for the maximum projected area in the direction of motion. A reason for this could be the asymmetry of the sail cross-section around mid-chord, as discussed above. The much larger camber close to the mast may make the flow that is slightly angled (sheet angle 80°) relative to the sail normal more efficient in creating resistance to the flow, thus producing more drive. This effect is not seen in the light wind case, however, so it has to be related to the larger mast bend or sail stretching in the stronger wind. The tight kicker trim is most efficient even for the strong wind. In fact, the advantage seems even larger for this case. The side force coefficient is very small around 80°. It is slightly positive for the loose kicker trim, but slightly negative for the other two trims. The yaw moment coefficient is positive for all sheet angles and kicker trims. Particularly the tight kicker trim produces large moments. Whether or not this outweighs the advantage of the larger drive force can be evaluated in a VPP.

Although there is this small advantage in the drive force at 80°, there is very little support for "negative sailing". Smaller sheet angles lead to smaller drive forces, larger side forces and a larger yaw moment.

5 CONCLUSIONS

Although downwind sailing in cat-rigged dinghies, such as the Olympic ILCA 7, is very complex, no optimisation studies have been presented in the literature. A major reason for this is the lack of relevant aerodynamic data. This paper has presented detailed such data, which coupled with systematic hydrodynamic data will enable very accurate predictions of the downwind performance of the dinghy. The optimum course can be found, as well as the optimum sheet angle, heel angle and kicker setting. The data is publicly available at Zenodo (2023).

A rather detailed description of the experimental technique has been presented. In particular, the scaling of the mast and sail is dealt with at some length. It was shown that the full-scale sail cloth could be used also for the model, and that the correct bending of the mast could be obtained if the full-scale aluminum tubes were replaced by a stainless-steel rod. The Reynolds number of the tests was however a factor $\sqrt{7}$ smaller than in reality. The radius of the model mast was also slightly smaller.

Although the primary result of the project is the data base, some general conclusions could be drawn from the data. Thus, for the light wind case (4 m s^{-1} apparent wind speed at full scale) it was found that the 90° sheet angle and the tight kicker trim gives the largest drive force for all apparent wind angles. The tight kicker trim also produces the smallest side force. It also appeared that the yaw moment can be minimised ether by heel to windward or by releasing the kicker trim. For the strong wind case (7 m s^{-1} at full scale) the maximum drive force was found at 80° sheet angle and the tight kicker trim. There is little support for negative sailing in this data. Small sheet angles consistently show smaller drive forces, as well as larger side forces and yaw moments. Although the test case here is the ILCA 7, the results should be of interest to sailors of other cat-rigged dinghies in downwind sailing.

6 ACKNOWLEDGMENTS

The CFD computations were enabled by resources provided by the Swedish National Infrastructure for Computing (SNIC) at Linköping, partially funded by the Swedish Research Council through grant agreement no. 2018-05973.

The authors are indebted to Professor Rickard Bensow, who reviewed the MSc thesis which is the basis for this paper.

REFERENCES

Arrendondo-Galeana, A. and I. M. Viola (2018). "The Leading-Edge Vortex of Yacht Sails." In: *Ocean Engineering* 159, pp. 552–562. ISSN: 00298018. DOI: 10.1016/j.oceaneng.2018.02.029. URL: https://www.sciencedirect.com/science/article/abs/pii/S0029801818301781?via%3Dihub.

Barlow, J. B., W. H. Rae, and A. Pope (1999). *Low-Speed Wind Tunnel Testing*. Toronto, Canada: John Wiley & Sons, inc.

Beer, F. P., R. E. Johnston, J. T. Dewolf, and D. F. Mazurek (2012). *Mechanics of Materials*. New York, USA: McGraw-Hill.

Carrico, T. (2005). "A Velocity Prediction Proram for a Planing Dinghy." In: *17th Chesapeake Sailing Yacht Symposium, CSYS*. Annapolis, Maryland USA: Society of Naval Architects and Marine Engineers Chesapeake Section. DOI: 10.5957/CSYS-2005-014. URL: https://onepetro.org/SNAMECSYS/proceedings-abstract/CSYS05/2-CSYS05/D021S002R006/462967.

Day, A. and E. Nixon (2014). “Measurement and prediction of the resistance of a laser sailing dinghy.” In: *Transactions of the Royal Institution of Naval Architects. Part B, International Journal of Small Craft Technology* 156.B1, pp. 11–20. URL: https://pureportal.strath.ac.uk/en/publications/measurement-and-prediction-of-the-resistance-of-a-laser-sailing-d.

Eca, L. and M. Hoekstra (2014). “A procedure for the estimation of the numerical uncertainty of CFD calculations based on grid refinement studies.” In: *Journal of Computational Physics* 262.1 Apr, pp. 104–130.

Flay, R. G. J. (1992). *Wind tunnel tests on a 1/6th scale laser model.* Southampton, UK: Ship Science Report No 55, University of Southampton. URL: https://eprints.soton.ac.uk/46414/.

Fossati, F. (2010). *Aero-Hydrodynamics and the Performance of Sailing Yachts*. London, UK: Adlard Coles Limited.

Harrison, N. (2012). *Open water tow tests of a laser dinghy.* Auckland, New Zealand: Master’s thesis, University of Auckland.

Hoerner, S. F. (1965). *Fluid-Dynamic Drag.* California, US: Published by the author.

ILCA, I. L. C. A. (2023). *ILCA Class Rules - One Design*. URL: https://www.laserinternational.org/.

Larsson, L. and H. C. Raven (2010). *The Principles of Naval Architecture Series, Ship Resistance and Flow*. New Jersey, US: The Society of Naval Architects and Marine Engineers (SNAME).

Le Pelley, D. and P. Richards (2011). “Effective Wind-Tunnel Testing of Yacht Sails Using a Real-Time Velocity Prediction Program.” In: *20th Chesapeake Sailing Yacht Symposium, CSYS*. Annapolis, Maryland USA.

Lindstrand Levin, R. and L. Larsson (2017). “Sailing yacht performance prediction based on coupled CFD and rigid body dynamics in 6 degrees of freedom.” In: *Ocean Engineering* 144.1 Nov, pp. 362–373. DOI: 10.1016/j.oceaneng.2017.09.052.

Lindstrand Levin, R. and J. Peters (2014). *CFD prediction of the effect of heel and trim on the resistance of an Olympic dinghy.* Gothenburg, Sweden: M.Sc. Thesis in Naval Architecture and Ocean Engineering, Chalmers University of Technology. URL: https://odr.chalmers.se/items/eb4167c0-4e0c-47cb-bf3e-3360c56d8bda.

Magnander, G. (2022). *Aerodynamic Analysis of the Bi-Radial MKII Sail for the Olympic Sailing Class Dinghy ILCA 7.* Gothenburg, Sweden: M.Sc. Thesis in Naval Architecture and Ocean Engineering, Chalmers University of Technology. URL: https://odr.chalmers.se/handle/20.500.12380/305825.

Marchaj, C. A. (1979). *Aero-Hydrodynamics of Sailing*. London, UK: Adlard Coles Limited.

de-Meijer, T. (2014). *Hydrodynamics of a Laser class yacht from full-scale towing tests.* Auckland, New Zealand: Masters in Yacht Engineering at the Faculty of Engineering, The University of Auckland.

ORC (2021). *World Leader in Rating Technology*. URL: https://orc.org/.

Pennanen, M., R. Levin, L. Larsson, and C. Finnsgård (2016). “Numerical Prediction of the Best Heel and Trim of a Laser Dinghy”. In: *11th Conference of the International Sports Engineering Association, ISEA*. Delft, Netherlands: Procedia Engineering, 147, pp. 336–341. DOI: 10.1016/j.proeng.2016.06.304. URL: https://www.sciencedirect.com/science/article/pii/S1877705816307512.

Souppez, J.-B. R. G., P. Bot, and I. M. Viola (2021). “On the Effect of the Leading-Edge Separation Bubble on the Aerodynamics of Spinnakers.” In: *7th High Performance Yacht Design, HPYD*. Auckland, New Zealand.

Souppez, J.-B. R. G. and I. M. Viola (2022). “High-blockage correctons for circular arcs at transitional Reynolds numbers.” In: *Journal of Wind Engineering and Industrial Aerodynamics* 229. URL: https://www.sciencedirect.com/science/article/pii/S0167610522002355?via%3Dihub.

Viola, I. M. (2013). “Recent Advances in Sailing Yacht Aerodynamics.” In: *Applied Mechanics Reviews* 65, pp. 040000-1-040000–12. DOI: 10.1115/1.4024947.

Viola, I. M., S. Bartesaghi, T. Van-Renterghem, and R. Ponzini (2014). “Detached Eddy Simulation of a sailing yacht.” In: *Ocean Engineering* 90, pp. 93–103. DOI: 10.1016/j.oceaneng.2014.07.019. URL: https://www.sciencedirect.com/science/article/abs/pii/S0029801814002911?via%3Dihub.

Viola, I. M. and R. G. J. Flay (2009). “Force and pressure investigation of modern asymmetric spinnakers.” In: *International Journal of Small Craft Technology Transaction RINA Part B2* 151, pp. 31–40. URL: https://www.pure.ed.ac.uk/ws/portalfiles/portal/14074681/Viola_Flay_2009IJSCT.pdf.

Viola, I. M. and R. G. J. Flay (2010). “Pressure distributions on modern asymmetric spinnakers.” In: *International Journal of Small Craft Technology Transaction RINA Part B1* 152, pp. 41–50. URL: https://www.research.ed.ac.uk/en/publications/pressure-distributions-on-modern-asymmetric-spinnakers.

Wolfson Unit (2023). *Consultants to the marine and industrial aerodynamic sector.* URL: https://wumtia.soton.ac.uk/.

Zenodo (2023). *Data set of the ILCA 7 MKII sail coefficients for downwind sailing.* DOI: 10.5281/zenodo.7905073. URL: https://zenodo.org/record/7905074.